The IAC Stripe 82 Legacy Project: a wide-area survey for faint surface brightness astronomy

Jürgen Fliri[1,2]⋆ and Ignacio Trujillo[1,2]⋆

[1]*Instituto de Astrofísica de Canarias, c/ Vía Láctea s/n, E-38205 La Laguna, Tenerife, Spain*
[2]*Departamento de Astrofísica, Universidad de La Laguna, E-38206 La Laguna, Tenerife, Spain*

ABSTRACT

We present new deep co-adds of data taken within Stripe 82 of the Sloan Digital Sky Survey (SDSS), especially stacked to reach the faintest surface brightness limits of this data set. Stripe 82 covers 275 deg^2 within $-50° \leq$ RA $\leq +60°$ and $-1°.25 \leq$ Dec. $\leq +1°.25$. We discuss the steps of our reduction which puts special emphasis on preserving the characteristics of the background (sky + diffuse light) in the input images using a non-aggressive sky subtraction strategy. Our reduction reaches a limit of $\sim$28.5 mag arcsec^{-2} (3σ, 10×10 arcsec^2) in the r band. The effective surface brightness limit (50 per cent completeness for exponential light distribution) lies at $\langle \mu_e(r) \rangle \sim 25.5$ mag arcsec^{-2}. For point sources, we reach 50 per cent completeness limits (3σ level) of (24.2, 25.2, 24.7, 24.3, 23.0) mag in (u, g, r, i, z). This is between 1.7 and 2.0 mag deeper than the single-epoch SDSS releases. The co-adds show point spread functions (PSFs) with median full width at half-maximum values ranging from 1 arcsec in i and z to 1.3 arcsec in the u band. The imaging data are made publicly available at http://www.iac.es/proyecto/stripe82. The release includes deep co-adds and representations of the PSF for each field. Additionally, we provide object catalogues with stars and galaxies confidently separated until $g \sim 23$ mag. The IAC Stripe 82 co-adds offer a rather unique possibility to study the low surface brightness Universe, exemplified by the discovery of stellar streams around NGC 0426 and NGC 0936. We also discuss further science cases like stellar haloes and disc truncations, low surface brightness galaxies, the intracluster light in galaxy clusters and the diffuse emission of Galactic dust known as Galactic Cirrus.

Key words: atlases – catalogues – surveys – stars: general – galaxies: general – galaxies: interactions.

1 INTRODUCTION

There is a huge amount of astrophysical phenomena that remain still barely studied due to the lack of large (several hundreds of square degrees), multiwavelength and deep ($\mu_V > 28$ mag arcsec^{-2}) optical surveys. These unexplored astrophysical events are those which are very subtle and extend over large areas of the sky. For instance, little is known about the connection of the so-called 'optical cirrus' or diffuse light of our Galaxy (de Vries & Le Poole 1985; Paley et al. 1991) and the dust filamentary structure observed in the far-infrared full-sky surveys (i.e. Low et al. 1984). Also, only a relative small number of nearby galaxies have been probed with enough depth (e.g. Ferguson et al. 2002; Mouhcine et al. 2005; McConnachie et al. 2006; Mouhcine, Rejkuba & Ibata 2007; Martínez-Delgado et al. 2008; Radburn-Smith et al. 2011; Bakos & Trujillo 2012;

Trujillo & Fliri 2015) to explore the cosmological predictions (e.g. Bullock & Johnston 2005; Cooper et al. 2010; Font et al. 2011; Tissera et al. 2013) about the formation of the faint stellar haloes, tidal streams and ultra-faint satellites surrounding these objects. Similarly, only a handful of nearby galaxy clusters (e.g. Rudick et al. 2010; Giallongo et al. 2014; Montes & Trujillo 2014) have been observed with enough depth to start understanding the intracluster light (ICL) expected from a hierarchical assembly (e.g. Contini et al. 2014) of these cosmic structures.

In the last few years, there have been a few dedicated surveys designed to explore some of the above astronomical questions. To name a few: (1) a survey to explore stellar tidal streams in spiral galaxies of the Local Volume (Martínez-Delgado et al. 2010). This survey uses small ($d = 0.1$–0.5 m) robotic telescopes to observe stellar streams down to $\mu_V \sim 28.5$ mag arcsec^{-2}, establishing a first classification scheme for the tidal features. (2) The Pan-Andromeda Archaeological Survey (McConnachie et al. 2009) conducted at the 3.6 m Canada–France–Hawaii Telescope whose main aim is the

⋆ E-mail: jfliri@iac.es (JF); trujillo@iac.es (IT)

exploration of the stellar halo surrounding our neighbouring Andromeda galaxy. This survey explores 400 square degrees reaching the following optical depth for point sources: $g = 25.5$ and $i = 24.5$ mag (S/N = 10). (3) Using the same telescope, another deep and large (104 square degrees) survey is the Next Generation Virgo Cluster Survey (Ferrarese et al. 2012). Among its observational goals is the exploration of the ICL in our closest galaxy cluster. The depth reached with this survey is the following: $u = 26.3$ (S/N = 5), $g = 25.9$ (S/N = 10), $r = 25.3$ (S/N = 10), $i = 25.1$ (S/N = 10), $z = 24.8$ mag (S/N = 5) [point sources]. (4) The Dragonfly telescope has joined recently in the initiative of exploring large areas of the sky to faint surface brightness limits. This telescope uses an array of telephoto cameras reaching a surface brightness limit of $\mu_g \sim 29.5$ mag arcsec^{-2} on scales of 10×10 arcsec^2 (Merritt, van Dokkum & Abraham 2014). However, there has not been yet a plan for a general multipurpose deep survey expanding over a large area of the sky that allows a systematic analysis of the phenomena stated in the previous paragraph.[1] None the less, many of the above issues could be addressed with a proper reduction of the data collected along the celestial equator in the Southern Galactic Cap of the Sloan Digital Sky Survey (SDSS; York et al. 2000), known popularly as the 'Stripe 82' survey (Jiang et al. 2008; Abazajian et al. 2009).

The Stripe 82 survey is a 2°.5-wide region along the celestial equator ($-50° \leq$ RA $\leq +60°$, $-1°.25 \leq$ Dec. $\leq +1°.25$ for a total of 275 square degrees). This region of the sky has been imaged repeatedly approximately 80 times in all the five SDSS filters: *ugriz*. The Stripe 82 area is a perfect piece of the sky for exploring many of the astrophysical phenomena described above. First, is accessible for the vast majority of ground-based facilities, helping to create ancillary spectroscopic and photometric observations if needed. Secondly, for analysing the optical emission of the dust of our own Galaxy, it covers regions from low to high Galactic extinction (Schlegel, Finkbeiner & Davis 1998).

Around a third of all the available SDSS data in the Stripe 82 area (123 of 303 runs[2]) were originally combined by Annis et al. (2014). The goal of that co-addition was 'to use this deep survey to understand the single-pass data at its limits and to do science at fainter magnitudes or correspondingly higher redshifts' (Annis et al. 2014). This stack produced the following depths (50 per cent completeness limit for point sources): $u = 23.6$, $g = 24.6$, $r = 24.2$, $i = 23.7$, $z = 22.3$ mag with a median seeing of $\sim$1.1 arcsec. Depending on the band, this is around 1–2 mag deeper than SDSS single-pass data. In a second reduction of the Stripe 82 data, Jiang et al. (2014) combined all available runs; the major differences to Annis et al. (2014) were the amount of data used and a different treatment of the sky background using a 2D background modelling. Depending on the band, Jiang et al. (2014) used between 75 and 90 per cent of the data for their co-adds, reporting a gain of 0.3–0.5 mag in depth compared to the Annis et al. (2014) reduction.

The science foreseen for the previous co-additions of the Stripe 82 survey has been focused on 'point sources science' (i.e. Galactic

structure, photometric redshift computation, cluster finding, etc.). However, the real treasure of the Stripe 82 survey is not only related to the detection of 'point-like' sources but in a different unique aspect: the exquisite surface brightness depth that a proper combination of this sub-project of the SDSS can reach over a wide area. In fact, one of the particular aspects of the SDSS survey is that it has been conducted using drift-scan mode. This observational technique has proved to be very efficient avoiding many of the artefacts affecting the quality of the imaging. Consequently, the single-pass SDSS imaging is superb for studies of low surface brightness features (reaching down to $\sim$26.5 mag arcsec^{-2} through direct detection (3σ, 10×10 arcsec^2) and $\sim$28 mag arcsec^{-2} through profile averaging techniques; Pohlen & Trujillo 2006). These are remarkable numbers taking into account that the SDSS survey has been obtained with exposure integrations of 53.9 s using a 2.5 m telescope. Considering that, on average, any region of the sky in the Stripe 82 area has been observed 80 times, a simple calculation shows that an optimal combination (i.e. assuming all single passes were of the same quality) of the Stripe 82 would be able to reach $\sim$2.4 mag deeper than the regular SDSS. In practice, as we will show, only around 2/3 of the full available Stripe 82 data are useful (i.e. with reasonable seeing and darkness) for our purposes.

The goal of this paper is to provide to the entire astronomical community with a new reduction of the Stripe 82 data, especially designed to prevent the destruction of the low surface brightness features in the co-addition of the data set. Moreover, our new co-addition takes advantage of the full useful data available in the Stripe 82 area, closely doubling the one third used by Annis et al. (2014). This allows us to go around 0.1–0.3 mag deeper than before. Our data release includes not only *ugriz* images and catalogues of the Stripe 82 but also some ancillary products as stacked point spread function (PSF) stamps along the survey area plus an 'ultra-deep *r*-band' image of the survey obtained by the stacking of the *g*, *r* and *i* co-added images. All our data are fully available for the astronomical community through a dedicated webpage at http://www.iac.es/proyecto/stripe82. Through the paper, we will show some examples of the quality of the new reduction and some of the science that can be conducted with this co-addition. The paper is structured as follows: in Section 2 we introduce the data used in our reduction of Stripe 82 while the reduction pipeline is presented in Section 3. We assess the quality of the co-added data in Section 4 and describe the contents of the data release in Section 5. Section 6 offers some science cases which can be explored with the Stripe 82 data. We end the paper with the conclusions in Section 7.

2 DATA

Reduced images for all 303 runs covering Stripe 82 are available as part of the SDSS DR7 (Abazajian et al. 2009) in a data base called Stripe 82. We have accessed these data through the Data Archive Server (DAS). The quality of the 303 runs changes from optimal seeing, sky brightness and photometric conditions for 84 runs obtained between 1998 and 2004 to 219 additional runs where the conditions were poorer including worst seeing, bright moonlight and/or non-photometric skies. These last runs were obtained from 2005 to 2007 as part of the SDSS-II Supernovae Survey (Frieman et al. 2008).

SDSS data are taken in scans along lines of constant survey latitude defining an SDSS strip. Two strips called strip 'north' and 'south' are needed to fill the 2°.5 width of an SDSS stripe. The run coverage of Stripe 82 is inhomogeneous over the survey area, but generally rises from west to east. For the observations in the

---

[1] A survey that potentially could have been used for the above purposes would be the Canada–France–Hawaii Legacy Survey (Cuillandre et al. 2012), in particular with its Wide Synoptic branch (155 square degrees with the following depth: $u = 25.3$, $g = 25.5$, $r = 24.8$, $i = 24.4$, $z = 23.5$ mag; 50 per cent completeness for point sources). Unfortunately, the pipeline used for the reduction of this data set removes the low surface brightness features, producing obvious 'holes' around the brightest extended galaxies in the images.

[2] An SDSS run is a single continuous drift scan obtained on a single night.

Stripe 82 southern strip, the difference in coverage between the western and the eastern limit of the survey is about 25 per cent. The difference is smaller for the northern strip with about 15 per cent. The co-addition that we present in this paper uses all the data (i.e. the 303 available runs) explained above after removal of some very bad data as we will explain later on in Section 3.5. This is a major difference compared to Annis et al. (2014). In fact, they combined only the data taken until 2005 (mostly because that data were not available when they were doing their co-addition). Annis et al. (2014) co-addition includes a total of 123 runs with every piece of the Stripe 82 area observed between 15 and 34 times. For comparison, any region of the Stripe 82 in our co-addition is observed ∼50 times.

3 REDUCTION

3.1 Field layout

We process the Stripe 82 data in patches of 0.25 square degrees, covering 0.5 deg both in right ascension and declination. Each declination interval of Stripe 82 is covered by five bins, centred at Dec. = $-1°$, $-0°.5$, $0°$, $0°.5$, $1°$. The numbering scheme in right ascension starts in the western part of the survey, with the first fields centred at RA = $310°.25$. With this general layout, we assign each field a unique identifier **fxxxy**, where the first three digits mark the running number of the field in right ascension (with **xxx** = 001 corresponding to a field centre at RA = $310°.25$), using a step size of 0.5 deg between different fields. The last digit refers to the declination bin with the declination moving from $-1°$ to $+1°$ in 0.5 deg steps when moving from **y** = 1 to **y** = 5. Field f0164 therefore refers to a field centre at (RA, Dec.) = $(317°.75, 0°.5)$.

Data are downloaded from the SDSS DAS using the SQL service CASJOBS to select all available images in the selected region. To avoid boundary effects, we chose a large enough search radius of 20 arcmin around each field centre in the selection. Data from the northern and southern strips of Stripe 82 are not processed separately but combined using the fpC images of all available runs for our co-adds. These *'corrected'* images have been bias-corrected, flat-fielded and largely removed from instrumental artefacts. A soft bias of 1000 counts has been added to allow the archival storage as unsigned integer. All fpC images have been astrometrically calibrated within SDSS, with an accuracy better than 45 mas rms (Pier et al. 2003). Each fpC image within the Stripe 82 data base has a tsField fits binary table associated with it, containing amongst other metadata, calibration parameters and information on the width of the PSF in the images.

3.2 Photometric calibration

We use the information contained in the tsField tables for the photometric calibration of the corrected fpC images. The values of the photometric zero-point ('aa'), extinction coefficient ('kk') and airmass ('airmass') were extracted for all five bands, yielding the photometric calibration of the fpC images according to

$$\frac{f}{f_0} = \frac{DN}{t_{\exp}} \times 10^{0.4 \times (aa + kk \times \mathrm{airmass})} \tag{1}$$

with f being the flux in the image, DN its corresponding count rate and f_0 the zero-point flux. Pogson magnitudes in the AB system are then calculated by

$$\mathrm{mag} = -2.5 \times \log \frac{f}{f_0}. \tag{2}$$

Before deriving appropriate values for the sky brightness and corresponding gradients in each image, the fpC images have to be aligned photometrically. This is achieved by correcting each image for the effects of atmospheric extinction and setting all images to a common zero-point of $aa' = -24.0$ mag, irrespective of observation date or waveband. After subtraction of the soft bias of 1000 counts, we multiply each image by a correction factor c defined as

$$c = 10^{0.4 \times [(aa+24) + kk \times \mathrm{airmass}]}. \tag{3}$$

For the fluxes $f' = c \times f$ and count rates $DN' = c \times DN$ in the corrected, photometrically aligned frames, the calibration equations take the following form:

$$\frac{f'}{f_0} = \frac{DN'}{t_{\exp}} \times 10^{0.4 \times aa'} \tag{4}$$

and

$$\mathrm{mag} = -2.5 \times \log \frac{f'}{f_0} \tag{5}$$

with a unique zero-point $aa' = -24.0$ mag.

3.3 PSF information

The SDSS photometric pipeline PHOTO fits various profiles for point and extended sources to objects detected in the fpC frames. All this information is used to obtain values for the shape and width of the PSF and its corresponding errors. As we use the PSF information primarily to discard certain images with large PSF widths from the individual stacks, we extract the PSF information from the tsField calibration tables (parameter 'psf_width').

3.4 Sky subtraction

To reach the very low surface brightness values we aim to achieve with our Stripe 82 co-adds, we have to determine the sky background in the single images to a high accuracy. Having measured sky values and their dispersion in the images, we are then able to discard images with large background values – taken under bad observing conditions with bad sky transparencies or during grey to bright time. In addition, we reject images with large variations of the sky background from the stacks. To get rid of point and extended sources which would affect the calculation of the sky background, we use SEXTRACTOR (Bertin & Arnouts 1996) to create object masks which include the background map-subtracted count rates of all objects detected in the SEXTRACTOR run. By applying a growth radius of 5 pixels to each pixel masked as object, we make sure that the faint wings of sources do not affect the estimation of the sky background. Finally, the soft bias-subtracted and flux-corrected fpC' images and corresponding object masks (transferred to binary images comprised of pixels with values equal 1 ' = sky' and 0 ' = object') are combined, yielding the input frames for the determination of the sky background. We obtain the sky values by placing 10^5 square apertures with side lengths of 21 pixels (or 8.3 arcsec) randomly in the images and measuring the median of the count rates in each box. The size of the apertures is chosen large enough to allow a robust measure of the median, but small enough to be affected by gradients in the sky background. κ-σ clipping of these 10^5 values yields a first determination of the sky value in the image and its dispersion. By repeating this procedure five times and averaging over the results, we finally obtain a very robust measurement of the sky background B in the images. Depending on the observing conditions, the background in the images is not completely flat but can

show gradients in both the scanning (RA) and perpendicular (Dec.) direction. However, as our main intent is on low surface brightness features, we subtract just a single value for the sky background and do not try to model it in 1D or 2D. In this way, we preserve as much as possible the characteristics of the low surface brightness objects. This is one of the major differences to previous reductions of Stripe 82 by Annis et al. (2014) and Jiang et al. (2014) which both apply background modelling in their reduction pipelines. For larger gradients and high background values, we apply several selection cuts which eliminate the data from the final stack and ensure that the data used in the co-addition have well-defined sky backgrounds.

3.5 Co-addition

Images with large sky backgrounds, notable sky gradients, large PSF widths, but also observations affected by clouds or bad transparency will degrade the quality and reduce the achievable depths of the co-added images. We therefore apply a couple of selection criteria to the images entering the stack. These criteria are based on the information gathered from the calibration tables (the width of the PSF and throughput information collected in the flux correction parameter c) and on information resulting from the sky determination (sky background B and its dispersion σ_B). Using the information from all the images, we calculate the κ-σ clipped mean and dispersion of the PSF ($\overline{\mathrm{PSF}}$, $\sigma_{\mathrm{PSF},s}$) and sky ($\overline{B}$, $\sigma_{B,s}$) in the image samples. For all the frames taken during the photometric runs until 2004, we also calculate the κ-σ clipped mean of the flux correction factors $\overline{c}$, and impose the following selection criteria for images entering the stack:

(i) $B < \overline{B} + 2 \times \sigma_{B,s}$
(ii) $\mathrm{PSF} < \overline{\mathrm{PSF}} + 2 \times \sigma_{\mathrm{PSF},s}$
(iii) $\sigma_B < \sigma_{\mathrm{lim}}$
(iv) $c < 1.30 \times \overline{c}$

with $\sigma_{\mathrm{lim}} = (0.5, 1.0, 1.2, 1.2, 0.5) \times \overline{c}$ for (u, g, r, i, z). This last criterion ensures that images whose throughput values deviate by more than 30 per cent from the mean of the photometric runs are discarded from the final stack. In this way, we eliminate non-photometric data taken under bad observing conditions. The criteria eliminate on average one third of the data with the fraction of bad data decreasing for redder wavebands. The median fractions of eliminated bad data are (39,41,34,26,23) per cent in (u, g, r, i, z), roughly constant over the survey area. This means that compared to Jiang et al. (2014), we only use ∼80 per cent of the data which passed their quality criteria for our co-adds.

All sky-subtracted and photometrically aligned images which pass the criteria are fed to SWARP (Bertin et al. 2002) for co-addition. SWARP takes the information on the World Coordinate System provided in the image header and projects the images on a regular grid with a pixel size of 0.396 arcsec before co-adding the images on a pixel-per-pixel basis. As we have already subtracted the sky from the images, we run SWARP without the sky subtraction option, choosing Lanczos3 as interpolation kernel during the regridding process which produces a tangent plane projection centred on the field centres. As output, SWARP yields the co-added image, calculated as unweighted median of the pixel values of all selected images, and a weight image providing the number of input frames contributing to the final stack on a pixel-per-pixel basis. The median ensures a robust removal of outliers and image defects.

Table 1. Median values of the PSF FWHM of the co-added data.

Band	FWHM (arcsec)
u	1.31
g	1.24
r	1.10
i	1.02
z	1.04
r_{deep}	1.08

4 DATA QUALITY

4.1 PSF values

We determined full width at half-maximum (FWHM) values of the PSF for all our co-adds using the PSFEX software (Bertin 2011). Image representations of the calculated PSFs are included in the data release (see Section 5.3). They can be plugged in easily to be used e.g. for model convolution within GALFIT (Peng et al. 2002), IMFIT (Erwin 2015) or similar applications. PSFEX relies on SEXTRACTOR catalogues in combination with small vignettes of detected objects in the images. Point sources are selected automatically by their determined half-light radius and brightness properties. We omitted any fitting or oversampling of the PSF to obtain its natural shape in the SDSS Stripe 82 fields, using the information of the whole 0.25 square degree co-add for the creation of deep PSFs in all bands.

In Table 1, we list the median values of the FWHM. As expected, the PSF is narrower in the redder bands with r, i and z showing values below 1.1 arcsec. The combination of the g, r and i bands (what we call r_{deep}) has a value of 1.08 arcsec. The u band has the broadest PSF. Still, with 1.3 arcsec, its value is sufficiently small for most ground-based astronomical studies. However, there is a strong dependence of the median width of the PSFs on the declination of the field centres; the dependence on right ascension is only mild (see Fig. 1). The fields centred at Dec. = +1° show similar PSF widths in all bands which could be up to 30 per cent larger than the respective median values. In these off-centre fields close to the northern limit of Stripe 82, the optics determine the PSF width. Also the fields at the opposite side of Stripe 82, centred at Dec. = −1°, are affected by the optics, albeit to a smaller degree than the northern fields. Here only the PSFs in the u and z bands show distributions shifted towards significantly larger values than the ones of the central fields close to Dec. = 0°.

4.2 Photometric accuracy

We investigated the accuracy of our photometric calibration by comparing aperture photometry of stars in our source catalogues with the SDSS standard star catalogue for Stripe 82 (Ivezić et al. 2007). The source catalogues are based on SEXTRACTOR photometry on our co-added images. They are described in more detail in Section 5.4. For the comparison, we used aperture magnitudes derived in fixed apertures of 30 pixels (11.88 arcsec) and required clean photometry flags which eliminate blended objects. From the standard star catalogue, we selected stars with photometric errors below 0.01 mag, i.e. stars brighter than (19.5, 20.5, 20.5, 20.0, 18.5) mag in (u,g,r,i,z). The quoted spatial variation of its photometric zero-points is not larger than ∼0.01 mag (rms). For each of the co-added images, we cross-correlated the catalogues with a search radius of 1 arcsec and fitted Gaussians to the magnitude differences. The zero-point
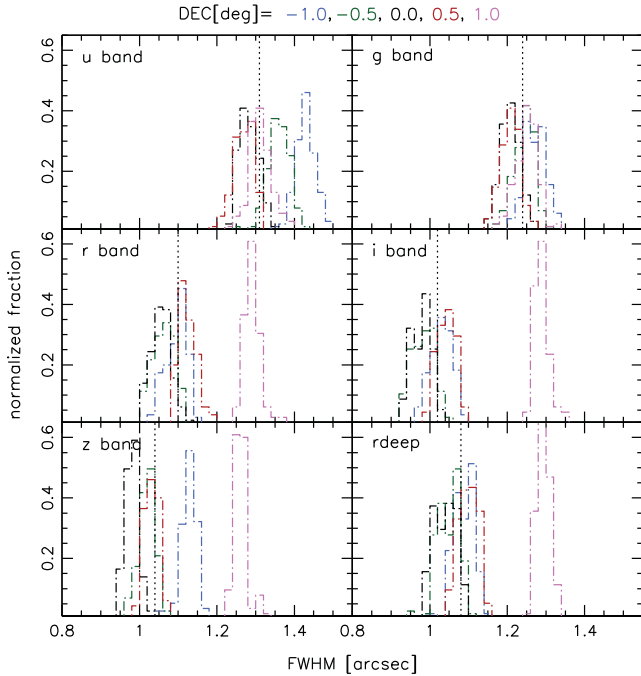
Figure 1. Distribution of PSF FWHM values along the Stripe 82 co-adds. The FWHM shows a strong dependence on the declination of the field centre. The median values in each band are indicated by vertical dashed lines.

4.3 Completeness simulations

To estimate the depth of our co-added images, we performed completeness simulations, adding point sources and extended sources of different profile shapes and effective radii to the co-added images and deriving the recovery fraction. We generated deep PSFs using the PSFEX software package which represent the input objects for the point source simulation. PSF convolved frames of the extended sources were constructed using GALFIT. To avoid crowding effects, single simulation runs consisted in adding between 250 and 500 objects to the images depending on the effective size of the objects. These runs were repeated multiple times to a total number of 5000 objects being injected in the images per filter and size-brightness combination.

Input objects were detected and measured by SEXTRACTOR, requiring 3σ detections with 3 connected pixels lying a factor of 1.74 above the rms value of the background for each pixel. For the background determination, we used a mesh size of 20 pixels and a background filter of 3 pixels width. Input objects were counted as detected if input coordinate and the SEXTRACTOR detection agreed within 1 arcsec.

Fig. 2 shows the detection maps (recovery fraction as a function of input magnitude and effective radius) for extended sources with de Vaucouleur and exponential surface brightness profiles and effective radii ranging from $\log(R_{\mathrm{E}}[\mathrm{arcsec}]) = -1.0$ to $\log(R_{\mathrm{E}}[\mathrm{arcsec}]) = +2.0$. For the exponential profiles, we include the lines of equal effective surface brightness $\langle\mu_{\mathrm{e}}\rangle$, calculated as

$$\langle\mu_{\mathrm{e}}\rangle = m_{\mathrm{T}} + 5 \times \log(R_{\mathrm{E}}) + 1.995 \tag{6}$$

for galaxies with a total luminosity m_{T} and an effective radius R_{E}. As Fig. 2 shows, we reach $\langle\mu_{\mathrm{e}}\rangle \sim 25.5$ mag arcsec^{-2} at the 50 per cent completeness level in the r band. The 50 per cent completeness values for the other bands are (25, 26, 25, 24) mag arcsec^{-2} in (u, g, i, z).

We compared the depth of the IAC co-adds with the Stripe 82 co-adds of the same area of Annis et al. (2014), available as runs 10006 and 20006 from the SDSS data archive, as well as with the SDSS DR7 single-epoch images. Both the Annis et al. co-adds and the DR7 data were aligned photometrically to the IAC co-adds using the information provided in the tsField calibration tables.
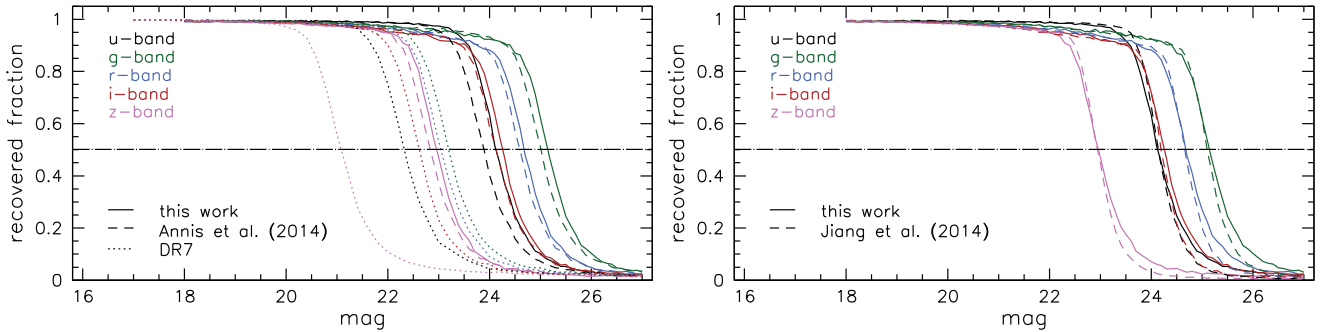
offsets determined in this way were then applied individually to the co-added images. Median values of the corrections were (0.03, 0.02, 0.02, 0.03, 0.03) mag in (u,g,r,i,z), i.e. they range between two and three times the zero-point accuracy of the standard star catalogue. These small zero-point variations can be ascribed to the accuracy of the calibration information provided for each fpC input image and the inclusion of images whose throughput factors deviate up to 30 per cent from the mean of the photometric runs (see Section 3.5).
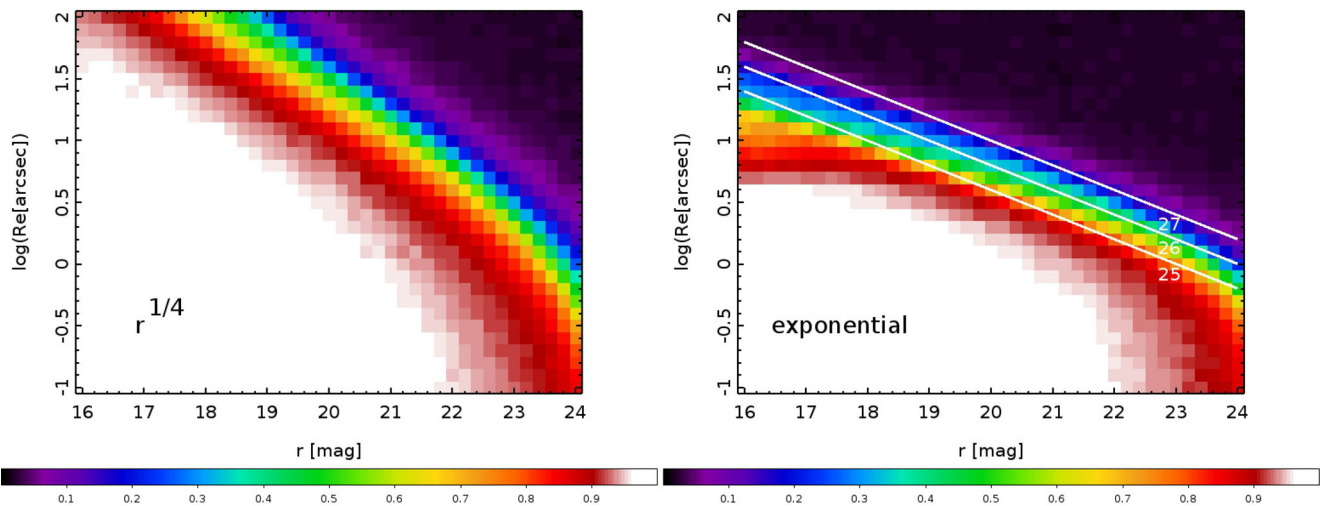
Figure 2. Detection map (recovery fraction as a function of input magnitude and effective radius) in the r band for simulated de Vaucouleur (left-hand panel) and exponential (right-hand panel) profiles with $\log(R_{\mathrm{E}}[\mathrm{arcsec}])$ ranging from -1.0 and $+2.0$. For the exponential profiles, we include the lines of equal effective surface brightness $\langle\mu_{\mathrm{e}}\rangle = 25, 26, 27$ mag arcsec^{-2} (from bottom to top). The 50 per cent completeness level lies at $\langle\mu_{\mathrm{e}}(r)\rangle \sim 25.5$ mag arcsec^{-2}.

Figure 3. Left-hand panel: recovery fraction of point sources as a function of input magnitude derived in a typical field of the Stripe 82 co-adds. The solid lines show the completeness curves for the IAC Stripe 82 co-adds. The comparison with the Annis et al. (2014) data is shown as dashed lines. The IAC reduction reaches between 0.1 and 0.3 mag deeper than the Annis et al. (2014) co-adds. Compared to the single-epoch DR7 release (dotted lines), the gain in depth for the detection of points sources ranges between 1.7 and 2.0 mag. Right-hand panel: recovery fraction of point sources as a function of input magnitude. The solid lines show the completeness curves for the IAC Stripe 82 co-adds; the comparison with the Jiang et al. (2014) data is shown as dashed lines. The depth of both reductions is similar in all bands.

Table 2. 50 per cent completeness limits for points sources, derived for all three reductions of the Stripe 82 data set. For reference, we give also the determined values for the single-epoch SDSS DR7 release and the gain in depth of the IAC co-adds presented in this work.

Band	DR7	Annis et al.	Jiang et al.	IAC	Gain
u	22.3	23.9	24.2	24.2	1.9
g	23.2	25.0	25.1	25.2	2.0
r	23.0	24.6	24.7	24.7	1.7
i	22.6	24.2	24.2	24.3	1.7
z	21.1	22.9	23.0	23.0	1.9

PSFs have been created in the same way as for the IAC co-adds. Fig. 3 shows the recovery fraction of point sources as a function of input magnitude, derived in a typical field of the Stripe 82 co-adds. The gain in depth relative to the single-epoch DR7 observations is around 1.7 mag in *r* and *i* and 1.9–2.0 mag in the *u*, *g* and *z* bands. In the *g* band, we reach a 50 per cent completeness limit of 25.2 mag. Compared to the Annis et al. (2014) data, the IAC co-adds reach deeper; the gain in depth ranges from 0.1 mag in the *r*, *i* and *z* bands to 0.3 mag in the *u* band. The *g* band lies between these values with a gain of 0.2 mag (see Fig. 3, left-hand panel).

For the comparison with the Jiang et al. (2014) data, we proceeded slightly differently. As their reduction included a 2D modelling of the sky background by fitting a hyperplane to the data, the rms in their images and hence the detection threshold are biased towards smaller count rates, making a comparison of the recovery rate difficult. We therefore decided to apply the 3σ threshold as determined by SEXTRACTOR for the IAC co-adds also for the SEXTRACTOR runs on the Jiang et al. (2014) co-adds which allows a one-to-one comparison of the detection efficiency. For these completeness simulations, we again aligned the Jiang et al. (2014) data photometrically to the IAC co-adds using the provided zero-points and created PSFs in the same way as for the IAC co-adds.

The depth of the IAC and Jiang et al. (2014) co-adds is similar in all bands, i.e. 0.1–0.3 mag deeper than the Annis et al. (2014) data (see Fig. 3, right-hand panel). Interestingly, we did not notice the 0.3–0.5 mag difference in depth between Jiang et al. (2014) and Annis et al. (2014) as reported in Jiang et al. (2014), derived as the magnitude at which the magnitude error exceeds 0.22 mag. We list our determined 50 per cent completeness values of all three Stripe 82 reductions and the DR7 single-epoch data in Table 2.

Simulations of extended objects follow the same trend as shown for the point sources, i.e. the data of Annis et al. (2014) being slightly shallower than the IAC and Jiang et al. (2014) data. Note, however, that this comparison gives only a lower limit on the difference in depth for extended objects between our and previous reductions. As the simulated objects are ingested in the final co-adds, the results only reflect the differences in the noise properties between the co-added images. They do not account however for differences in the reduction process which could affect the characteristics of extended objects, especially at the low surface brightness limit. This is exemplified in Fig. 4 which shows a field with intense emission of Galactic Cirrus (see Section 6.5) in our reduction and the reduction by Jiang et al. (2014). Both images show large differences in the brightness of the dust clouds. In the regions with maximum emission, the intensity in the Jiang et al. (2014) data is reduced by roughly a factor of 2 compared to our data. This reduction in flux originates presumably from differences in the treatment of the sky background in the input images. Our reduction subtracts just a single background value and therefore preserves the characteristics of the background composed of sky and diffuse light. Jiang et al. (2014) on the other hand subtract a 2D model of the background which can potentially misidentify faint astronomical objects as sky background and eliminate them from the reduced images or alter their fluxes.

5 DATA RELEASE

The data products of the Stripe 82 reduction are released through a dedicated webpage at http://www.iac.es/proyecto/stripe82. The release contains the co-added data in 5+1 bands, sky-rectified versions of the co-adds, corresponding exposure time maps, image representations of the PSF for each co-add and catalogues of point and extended sources.

5.1 Co-adds

The co-added data are provided in patches of 0.5×0.5 square degrees. In this way, five images cover the full range of declination ($-1.25°$ to $+1.25°$) at a certain right ascension in the Stripe 82 region. The data are calibrated to a common zero-point of 24 mag for all bands. AB magnitudes can be derived from the data via

$$\text{mag} = -2.5 \times \log\left(\frac{DN}{t_{\text{exp}}}\right) + 24.0, \tag{7}$$
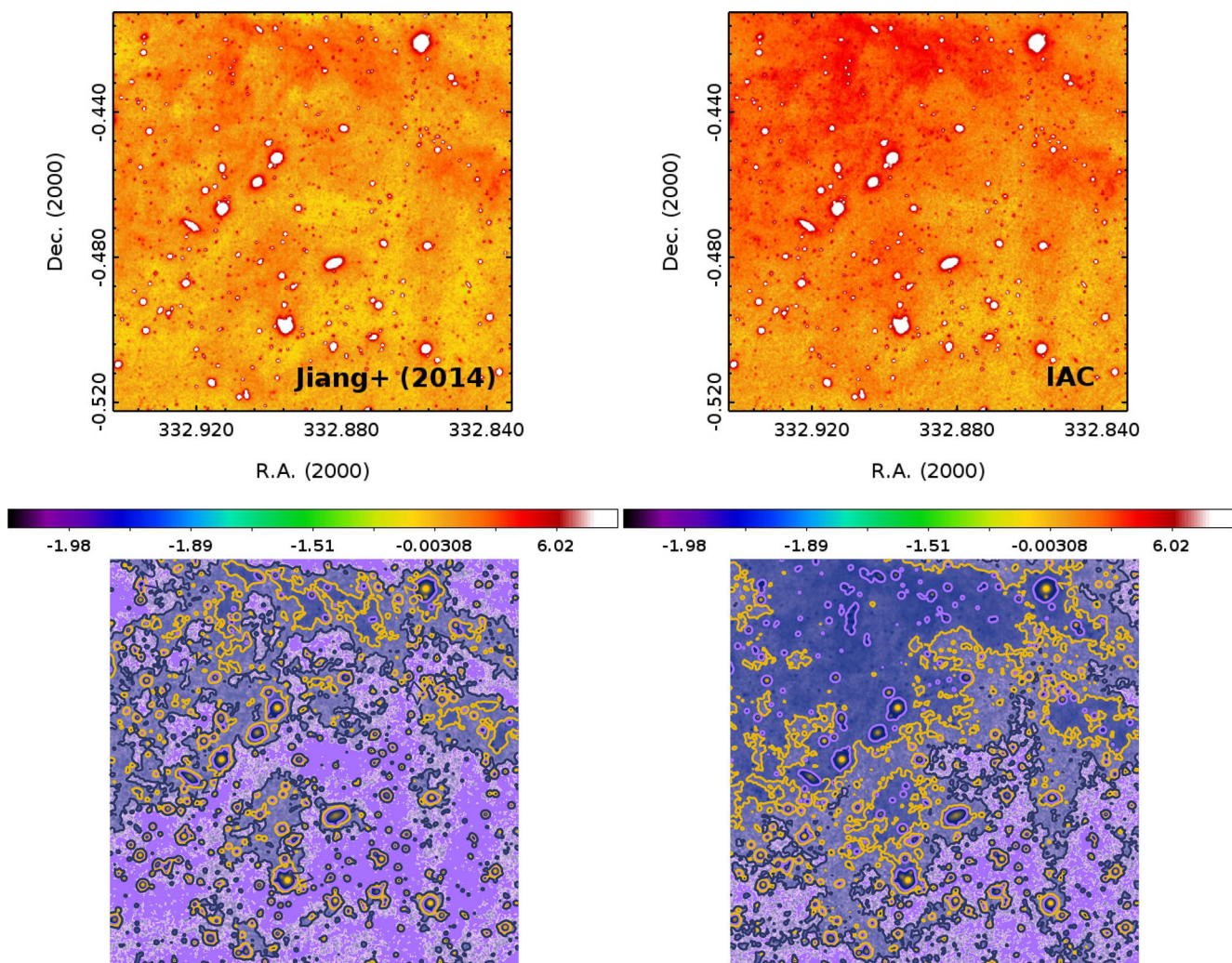
Figure 4. Comparison of a field showing intense emission of Galactic Cirrus in Jiang et al. (2014, left-hand panels) and our data (right-hand panels). The top panels show the co-adds in the *r* band in the same dynamic range. Both images were photometrically aligned to the same zero-point. Additionally, we applied corrections of +0.16 and +0.34 *DN* to the Jiang et al. (2014) and our image, respectively. These values correct for a slight negative offset of the background in pure sky regions. They have been determined as the median of the count rates in selected empty regions in the field. The bottom panels show the surface brightness distribution of the Galactic Cirrus in both images. Contour values are 25, 26 and 27 mag arcsec^{-2}. Compared to our images, the cirrus emission is largely reduced in the Jiang et al. (2014) data, presumably due to differences in the background treatment in the reduction process.

where $t_{exp} = 53.907\,456$ s refers to the exposure time of a single SDSS image and *DN* to the counts measured in the co-add.

Each co-added image has an exposure time map attached to it which yields for each pixel the number of single images $n(x, y)$ entering the stack. The effective exposure time in each part of the image is given by the product $n(x, y) \times t_{exp}$.

Additionally, we provide images representing the average of the *g*, *r* and *i* co-adds which, for a flat object spectral energy distribution, can be regarded as deep *r*-band co-adds. As the calibration gets destroyed during this process, above equations are invalid for the deep *r*-band (r_{deep}) images. Nevertheless, the gain in depth of 0.2–0.3 mag compared to the single co-adds can give valuable insights into low surface brightness features close to the detection limit of the survey.

5.2 Sky-rectified co-adds

Small gradients in the background of similar shape and amplitude are still apparent in the co-adds from Annis et al. (2014) and our

work, predominantly along the Dec. direction. As the reduction of Jiang et al. (2014) included a 2D modelling of the sky background in the input SDSS images, their co-adds show the smallest gradients. To preserve as much as possible the intensity and shape of objects at low surface brightness, we decided to characterize the sky properties of the input SDSS images by a single value and tackle larger gradients by the measured variance of the sky background over the image. Remaining small gradients are treated in the co-adds at much higher signal-to-noise (S/N) than in the input SDSS images. In this way, the probability of confusing sky background and astrophysical objects at low surface brightness is reduced.

For sky-rectified versions of our co-adds, we proceed as follows. Object masks are created independently for the co-adds in each filter. Here, we put large emphasis on conservatively masking the haloes of stars and galaxies but also the areas with Galactic Cirrus or diffuse low surface brightness emission. The masks also include the extended PSF wings of bright stars and ghost artefacts. We then calculate the κ-σ clipped mean of the lines perpendicular to the direction of the gradient, i.e. the RA direction, and subtract the
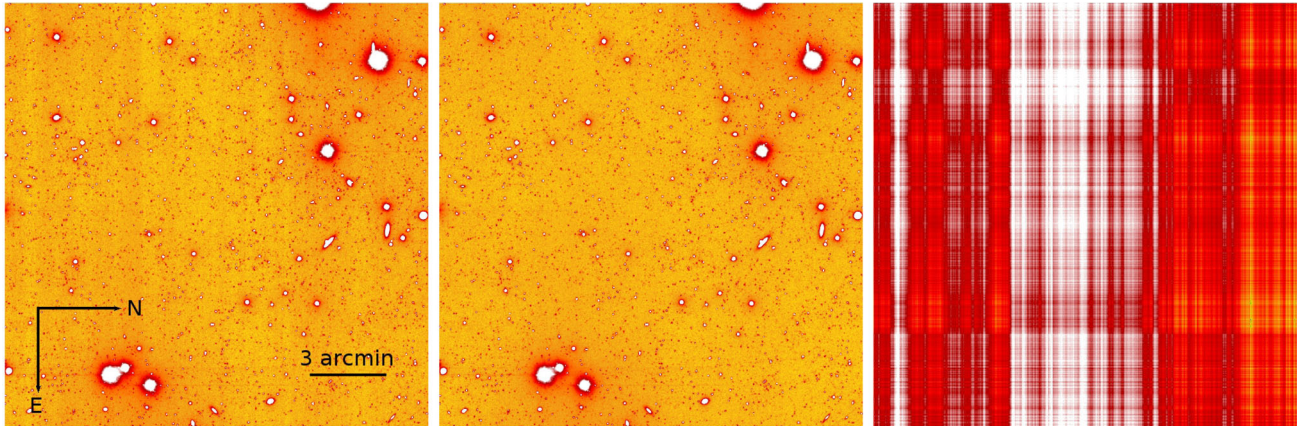
Figure 5. Example of the sky rectification method. Left-hand panel: the original co-add in r_{deep} shows small gradients along the Dec. direction. Middle panel: sky-rectified version of the same image. Right-hand panel: correction applied to the data; the frame shows the expected pattern of vertical and horizontal lines, but no imprints of objects.

value from the count rates in these columns. To eliminate small inhomogeneities in the perpendicular direction, we calculate the κ-σ clipped mean of the rows and subtract it; this step uses the already column-corrected image from the previous step as input. As example resulting from this method we show in Fig. 5 the original co-add, the sky-rectified version and the difference of both, i.e. the correction applied to the data. The correction frame shows the expected pattern of vertical and horizontal lines with no additional features related to objects in the field of view. Our tests have shown that the method is flux-conserving and preserves the quantities of low surface brightness features like Galactic Cirrus.

5.3 Deep PSFs

Representations of the PSF are provided for each co-add in the five SDSS bands plus the r_{deep} images. The PSFs are calculated using the PSFEX software which selects point sources from SEXTRACTOR catalogues, normalizes and combines them to a robust mean PSF for a particular field. The selection of point sources is done in an automatic way using the half-light radius and luminosity information included in the SEXTRACTOR catalogues. Depending on the filter and the location of the field within Stripe 82, between 300 and 2000 point sources are used for the determination of the PSF, with the smallest numbers applying to the u band, as expected. The rms variation of the FWHM of the PSF across our 0.25 square degrees fields ranges between 1 per cent (median value) in the central fields close to the optical axis and up to 5 per cent (median value) in the northern fields at Dec. $= +1°$, with the spread being largest in the i band and smallest in the u and g bands. The rms is mostly dominated by the variation of the PSF along the Dec. direction, causing generally broader PSFs in the off-centre fields (see Section 4.1 and Fig. 1). As each portion of the Stripe 82 co-adds is composed of images sampling the whole range in positions on the CCD along the scanning (RA) direction, the PSF dependence on the RA in the individual co-adds is weak.

The properties of stellar haloes and the faint outskirts of galactic discs can be largely influenced by the wings of the stellar PSF (e.g. Zibetti, White & Brinkmann 2004; Sandin 2014; Trujillo & Fliri 2015). To estimate this effect in the Stripe 82 data, we provide ultra-deep PSFs reaching out to 8 arcmin in radius and extending over 20 mag in dynamical range. The ultra-deep PSFs were created by combining the PSFs of bright saturated stars and PSFEX-generated
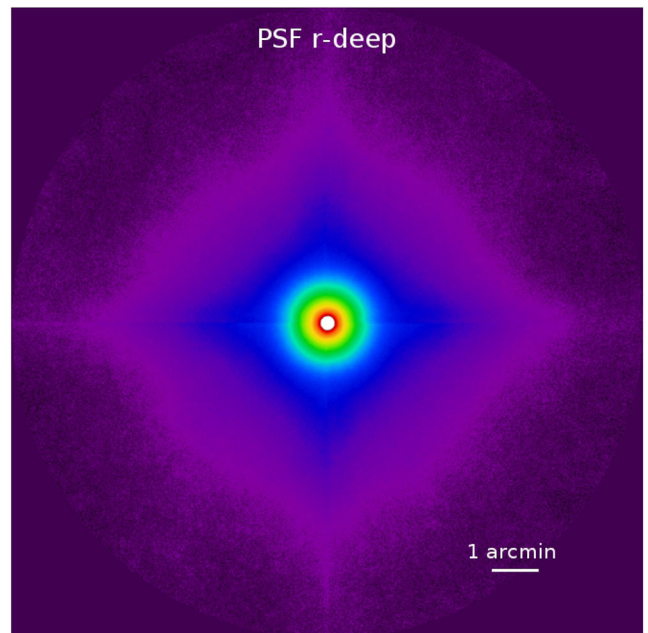

Figure 6. Ultra-deep PSF in the r_{deep} band. The PSF was obtained by combining the PSF of bright saturated stars for the outer part with PSFEX-created high-S/N PSF for the inner part. The dynamical range of the PSF extends over 20 mag.

PSFs of certain fields. For the saturated part, we selected 102 bright stars with $6 < R < 8$ mag within the Stripe 82 region from the United States Naval Observatory B1.0 catalogue (Monet et al. 2003). The stellar images were aligned to a common grid based on the catalogue positions and normalized to a common flux by using their catalogue magnitudes: B was used for the u and g bands, R for the r band, and I for i and z bands. In every band, the final PSF was obtained by median-combining each stack of images. For the central saturated part of the PSF, we use a high-S/N PSF created by PSFEX on a frame covering several Stripe 82 fields. After matching the profiles of saturated and non-saturated PSFs to align the flux scaling, both PSFs were combined to the ultra-deep PSF. As example, we show the ultra-deep PSF in r_{deep} in Fig. 6.

5.4 Catalogues

We created catalogues of point and extended sources for the whole survey area which are included in the release of the Stripe 82 data products. The catalogues are based on SEXTRACTOR photometry; they include the positions, matched aperture luminosities, effective radii and structural parameters like the moments of the brightness distribution.

The catalogues contain objects being detected at least at the 3σ level in g, r and i, requiring 3 connected pixels showing a 1.74σ excess above the background in all three bands. Objects are detected in each band separately; detections within a search radius of 1 arcsec are merged to a common detection later on. Kron apertures and structural parameters of the common detections in g, r and i are determined in the deep r-band image which yields a robust measurement of these parameters. To obtain the object fluxes in matched apertures, SEXTRACTOR is rerun in double-image mode for each band on the Kron apertures measured in r_{deep}. We also provide the object fluxes in fixed apertures of 5, 10, 20 and 30 pixels in diameter (1.98, 3.96, 7.92, 11.88 arcsec), useful to estimate the aperture correction for point sources. The correction between the Kron magnitudes and the magnitude measured in an infinite aperture depends on the waveband and the field within Stripe 82, but usually is of the order of a few hundredth of a magnitude between 0.02 and 0.05 mag.

To separate point from extended sources, we rely on a combination of SEXTRACTOR runs in (g, r, i, z, u) and DAOPHOT II/ALLSTAR (Stetson 1987) runs on the r_{deep} images. Although of slightly broader PSF than the i or z band, the r_{deep} images are best suited for this task as the gain in depth allows us to enhance the magnitude limit for a proper separation of stars and galaxies. Whereas SEXTRACTOR has its advantages in the photometry of extended sources, the DAOPHOT package is optimized for point sources. The combination of both methods allows, especially at fainter magnitudes, a cleaner separation between extended and point-like objects than one based on the CLASS_STAR or FLUX_RADIUS parameters returned by SEXTRACTOR. The DAOPHOT runs yield an estimate of stellarity or point-likeness encoded in the two parameters which are output for each source, SHARP (providing an estimate of the concentration of the source) and CHI (providing an estimate of the goodness of fit of the object's profile to the stellar PSF). For point-like sources, we require |SHARP|<0.5 and CHI<7.5. Objects which fulfil these criteria in r_{deep} are assigned to the catalogue of point-like sources. All other objects from the combined g, r and i catalogue are assigned to the extended object catalogue.

Fig. 7 shows colour–magnitude diagrams (CMDs) of point-like sources for 10 adjacent fields. The CMDs show the signatures of different Galactic populations like stellar halo and thick disc at $g - r \sim 0.4$ or M stars in the thin disc, thick disc or the halo at $g - r \sim 1.5$. The separation between stars and galaxies works well until $g \sim 23$ mag. At fainter magnitudes, the contamination by extended objects is starting to get larger. To assess the quality and the limit of the star/galaxy separation more closely, we created colour–colour plots of the stellar catalogues. In Fig. 8, we show $(g - r)$ plotted against $(r - i)$ for the point-like sources, split into different bins in g-band magnitude. The stellar sequences get broader for fainter magnitude bins due to larger photometric errors. They are well defined until $g \sim 23$ mag with only a small fraction of outliers, the majority of them presumably being misclassified galaxies. Beyond this limit, the contamination of the point source catalogue gets worse.
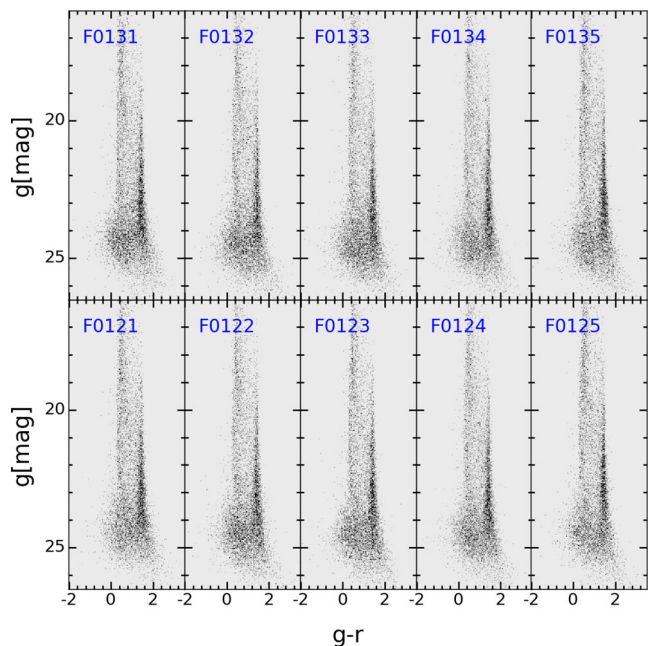

Figure 7. $[g, g - r]$ colour–magnitude diagrams of 10 adjacent IAC Stripe 82 fields covering 2.5 square degrees in total. Various sequences can be attributed to different Galactic populations like thin and thick disc or the stellar halo. The contamination by extended sources is small until $g \sim 23$ mag.
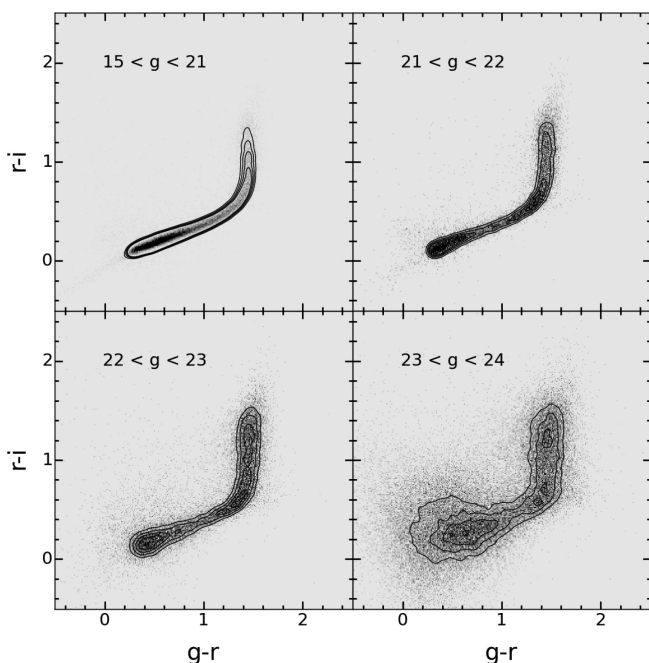

Figure 8. $[g - r, r - i]$ colour–colour diagrams for point-like sources in 10 square degrees of Stripe 82, split into different bins in g-band magnitude. For the contours, a Gaussian smoothing of three times the binning size in colour (0.01 mag) has been applied. The contour levels mark two, three, four, five sources per binning interval. The stellar locus is well defined with only a small contamination by QSOs and extended sources until $g \sim 23$ mag.
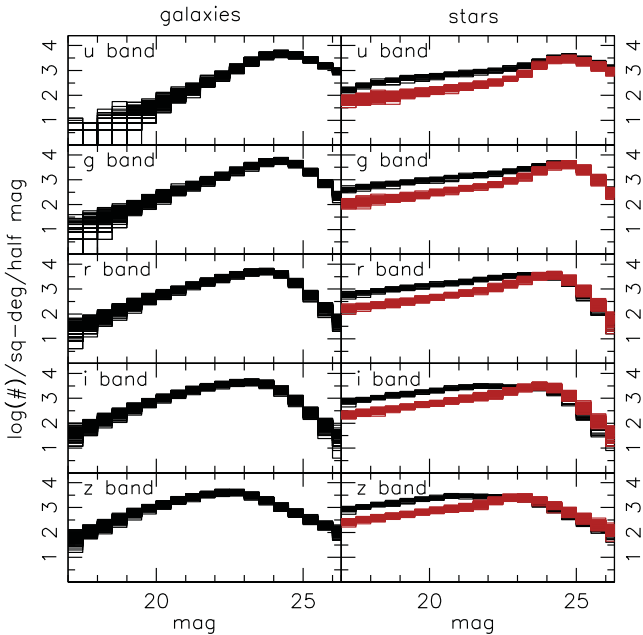
Figure 9. Number counts of point and extended sources for 100 fields covering 25 square degrees in total. The fields are grouped around two different Galactic coordinates, $(l,b) = (50°, -30°)$ (black lines, right-hand panel) and $(l,b) = (70°, -50°)$ (red lines, right-hand panel).

5.5 Number counts

5.5.1 Point sources

In Fig. 9, we show the number counts of point and extended sources for 100 fields covering 25 square degrees in total. The fields are grouped around two different Galactic coordinates at $(l,b) = (50°, -30°)$ (black lines, right-hand panel) and $(l,b) = (70°, -50°)$ (red lines, right-hand panel). In the stellar counts, this is reflected as overall decline in density for higher latitudes. The stellar counts are well described by a power-law rise towards fainter magnitudes until the turn-over when incompleteness starts to set in. The bump-like excess of counts seen in all bands, with its maximum at e.g. $g \sim 25$ mag, is due to galaxies being misidentified as stars. The values of the turn-over magnitudes in the five bands agree with the results of the completeness simulations. In these simulations, we used the same detection criteria. However, we did not require detections in multiple bands nor included colours for the simulated objects.

5.5.2 Extended sources

The number counts of galaxies are shown in the left-hand panel of Fig. 9. The broadness of the number counts distribution shows the field-to-field variations one can expect from the Stripe 82 catalogues. The presence of bright, saturated stars and/or large galaxies affects the number counts in some co-adds. These brighter objects affect the normalized counts in two ways, sometimes by reducing the accessible area in the field, the other time by enhancing the detection limit in their surroundings. Depending on the brightness of the object, the affected areas could be several square arcminutes in size. Due to smaller number densities at the bright end, the variance of the galaxy counts is larger than the ones of the stellar counts.

Another way to look at the galaxy populations is to plot their effective radii against their luminosities. In Fig. 10, we show the
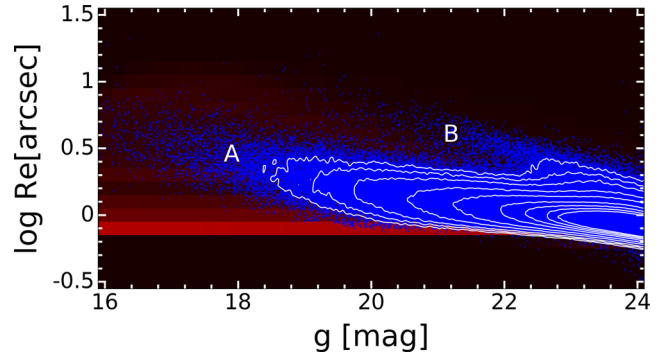

Figure 10. Size–luminosity relation for extended objects in the *g* band. Shown in blue are objects classified as non-point-like in the Stripe 82 catalogue. The labels 'A' and 'B' mark the main relation and the sequence of partially resolved galaxies, respectively. The sources are overlaid on the completeness map for the simulation of exponential profiles, representing the recovery fraction based on recovered sizes and luminosities of the input objects.

measured size–luminosity relation in the *g* band. Most of the galaxies fall on the main relation. A second, sparsely populated sequence (labelled 'B' in Fig. 10) shifted towards larger radii is populated by two classes of objects. The first class consists of partially resolved nearby spiral galaxies which have been split into multiple objects. The measured apertures trace spiral arms or brighter knots like star-forming regions in these galaxies rather than the galaxy as a whole. The second class populating this sequence is made of faint galaxies in the haloes of brighter stars which have both their size and luminosity been affected by the presence of the bright object nearby. The main relation (labelled 'A' in Fig. 10) follows the known correlation that brighter galaxies tend to have larger effective radii. At small effective radii, the relation saturates as the measured effective radii are limited by the size of the PSF. This is also reflected in the completeness map from our simulations, which is underlaid on the distribution of measured galaxies. The completeness map gives the fraction of recovered sources based not only on recovered position but also on recovered sizes and luminosities. Comparing the completeness map with the detection maps in Fig. 2 shows that larger objects tend to be measured with smaller effective radii and fainter magnitudes, a result of their lower surface brightness and the effect of the noise in the images. The prominent row at $\log(R_E) = -0.1$ in the completeness map is due to input sources with effective radii smaller than the PSF size.

6 SCIENCE SHOWCASES

As indicated in the introduction, a survey like Stripe 82 allows us to address a number of astrophysical phenomena. In what follows, we will illustrate some specific scientific cases that can be explored with the reduction of the Stripe 82 we have conducted. These and other questions will be fully analysed in forthcoming papers: stellar haloes of disc and elliptical galaxies, tidal streams and satellite populations, low surface brightness galaxies, ICL, optical cirrus, etc.

6.1 Stellar haloes and disc truncations

Truncations in edge-on galaxies are known for a long time (e.g. van der Kruit 1979), but have been proven elusive in face-on galaxies. Two main families of models have been proposed for the origin of
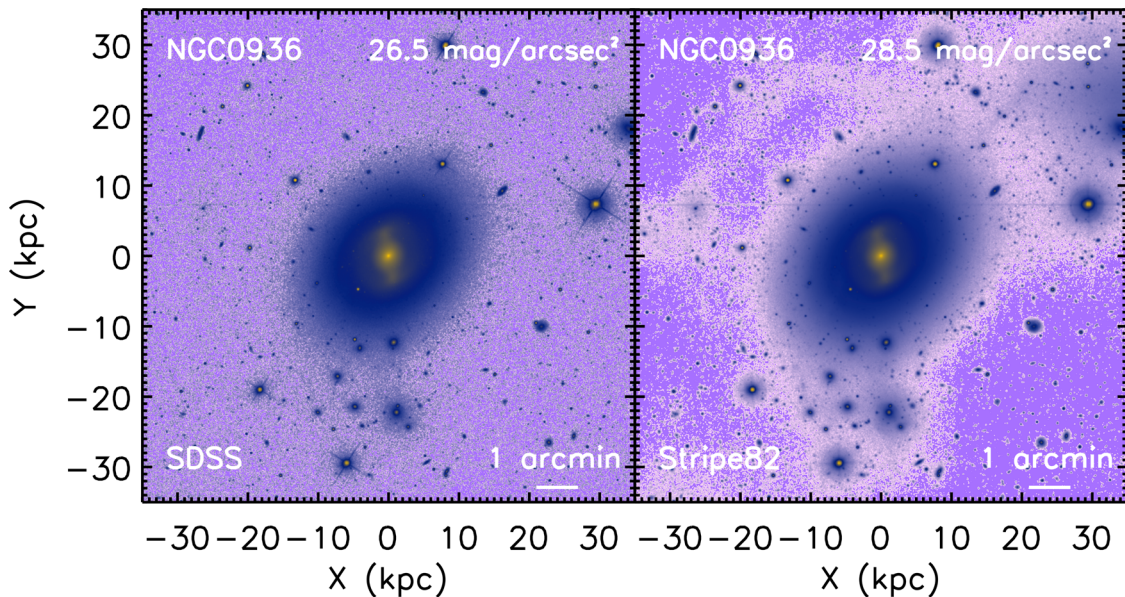
Figure 11. The effect of increasing the depth at observing nearby galaxies. The figure shows the galaxy NGC 0936 (the so-called Darth Vader's galaxy) in the *r* band. The galaxy is shown at two different surface brightness limiting depths: $\mu_r(3\sigma; 10\ \mathrm{arcsec} \times 10\ \mathrm{arcsec}) = 26.5$ and 28.5 mag arcsec^{-2}. The emergence of a faint tidal stream ($27 \lesssim \mu_r \lesssim 28$ mag arcsec^{-2}) in the stellar halo of this galaxy exemplifies the need of ultra-deep observations to explore the substructure prediction by the ΛCDM model.

truncations: suppression of star formation below a certain gas density threshold for local instability (Fall & Efstathiou 1980; Kennicutt 1989; Schaye 2004), and one in which the truncation corresponds to a maximum in the specific angular momentum distribution of the present disc, and might correspond to that in the protogalaxy (van der Kruit 1987).

The absence of stellar disc truncations in low-inclination spiral galaxies has been a matter of debate in the last decade. Martín-Navarro et al. (2014) argue that stellar haloes outshine the galaxy disc at the expected position of the truncations, forcing their studies to highly inclined (edge-on) orientations. Using a simple exponential disc plus stellar halo model based on current observational constraints, they show that truncations in face-on projections occur at surface brightness levels comparable to the brightness of stellar haloes at the same radial distance.

This view is supported by a recent study of halo truncations in 22 nearby, face-on to moderately inclined spiral galaxies, making use of the r_{deep} co-adds of our Stripe 82 reduction (Peters et al. 2015). Truncations are found in only three galaxies, an additional 15 galaxies are found to have an apparent extended stellar halo. Their simulations show that the scattering of light from the inner galaxy by the PSF can produce faint structures resembling stellar haloes, but in general this effect is insufficient to fully explain the observed haloes.

There is a long debate about whether stellar haloes are formed *in situ* during a monolithic collapse at early times (Eggen, Lynden-Bell & Sandage 1962) or are built up by the remnants of accreted substructures (Searle & Zinn 1978). Both models give very different predictions on halo mean age and metallicities, age and metallicity gradients, and the overall density gradient. The deep Stripe 82 data reach depths which allow, for the first time, to detect and characterize stellar haloes for a statistically meaningful ($\sim$100) sample of galaxies of different types. Studies like this will have immediate and important consequences for our understanding of galaxy formation and evolution.

6.2 Stellar streams

Λ cold dark matter (ΛCDM) models predict an increasing amount of substructure (stellar streams, shells, filaments) within the stellar haloes of galaxies when lowering the surface brightness threshold to values below 30 mag arcsec^{-2} (e.g. Bullock & Johnston 2005; Cooper et al. 2010; Font et al. 2011; Tissera et al. 2013). Consequently, the brightest streams will be in the reach of the surface brightness limits of $\mu_r \sim 28.5$ mag arcsec^{-2} we acquire in our Stripe 82 co-adds. Here we show two exciting examples of the possibilities and new discoveries Stripe 82 offers in this regard: an extended faint stellar stream around NGC 0936 (also known as the Darth Vader's galaxy) and the ongoing disruption of a dwarf satellite by the elliptical galaxy NGC 0426.

The stream around NGC 0936 (distance 19.8 Mpc) is seen as a huge loop surrounding one third of the galaxy and extending $\sim$30 kpc from the galaxy centre. With $27 \lesssim \mu_r \lesssim 28$ mag arcsec^{-2} and $(g - i) \sim 1.1$, the stream is close to the surface brightness limit of our co-adds. In Fig. 11, we show the stream, comparing the depth of the single-pass SDSS DR7 imaging (left-hand panel) versus the Stripe 82 *r* band (right-hand panel), smoothed with a boxcar average of 3 arcsec width. The surface brightness depth of the images has been estimated using the rms of the images in boxes of 10×10 arcsec^2 (i.e. around $10 \times$ FWHM) and corresponds to 3σ detections. At its visible end, the loop emerges into a diffuse object, presumably a dwarf galaxy undergoing tidal disruption and the progenitor of the stream. The galaxy has a bright core and seems quite extended; if the connection of the dwarf and NGC 0936 is confirmed, its distance would imply a size of $\sim$6 kpc in diameter. Its central surface brightness is $\mu(r, 0) = 21.4$ mag arcsec^{-2}; the surface brightness just outside the core is around $\mu_r \sim 26.3$ mag arcsec^{-2} with $(g - i) \sim 1.0$. These properties match some of the characteristics of the recently discovered class of ultra-diffuse galaxies (UDGs; see Section 6.3). However, as this system is presumably tidally disturbed, a relation to this type of objects is not straightforward.
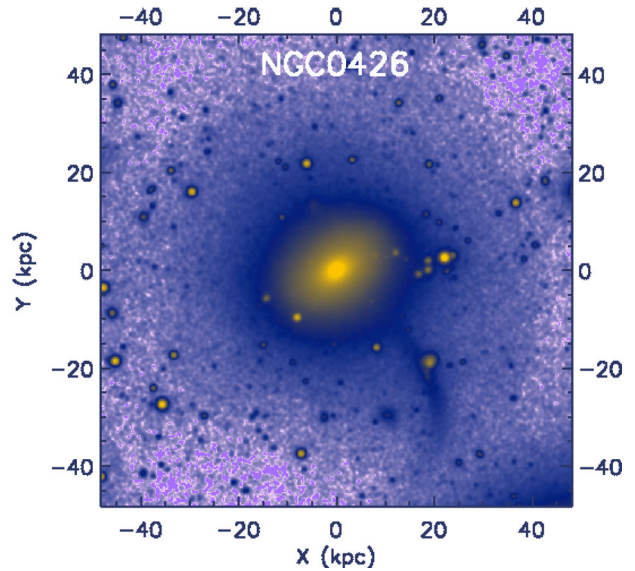
Figure 12. Left-hand panel: real colour composite image of NGC 0426 and its stream system. The main body of the dwarf satellite is still undergoing the disruption event. Two compact objects are located close to the suspected centre of the dwarf (marked by white horizontal lines). The colours of the compact sources differ significantly, with one having a colour quite similar to the one of the stream. The second one is much redder, suggesting it being a background galaxy or a globular cluster. Right-hand panel: NGC 0426 in the *i* band, filtered with a median kernel of 3 arcsec side length. The stream is fully embedded in the stellar halo and the shell system around the galaxy.

As second example we show the stellar stream around NGC 0426, a redshift $z = 0.017$ elliptical galaxy hosting an AGN (see Fig. 12). The stream is relatively bright reaching $\mu_g \sim 24.9$ mag arcsec^{-2}. In the Stripe 82 images, it is traced from the centre of NGC 0426 until projected distances of ~ 45 kpc. The system is seen in the state of ongoing disruption; towards the centre of the presumed progenitor (at $x = 18$ kpc, $y = -21$ kpc in galactocentric coordinates), the images show two dense cores with largely different colour characteristics. One of the compact cores has a colour $(g - i)\sim 1.1$, only slightly redder than the colour of the stream $(g - i)\sim 1.0$. The second core is much redder with $(g - i) > 2$ which could point to a globular cluster or a background galaxy seen projected on the stream. We calculated surface brightness profiles for NGC 0426 using the IRAF/ELLIPSE task. The profiles are shown in Fig. 13; outside a radius of 2 arcsec (0.7 kpc), the colour is constant with $(g - i)\sim 1.3$. At an isophotal radius $r = 31$ arcsec (11 kpc), the profiles steepen; beyond this radius, the ellipticity values decline from their maximum at $\epsilon = 0.3$ close to $\epsilon = 0$ at $r = 60$ arcsec (21 kpc). The mean colour shows subtle changes after the break, however remains redder than the main part of the stellar stream throughout the profile. It is worth noting that a comprehensive analysis of the colour gradient will require an exploration of the effect of the PSF on the galaxy light distribution. In Fig. 12 (right-hand panel), we show the *i*-band image of NGC 0426 which impressively reveals the extent of the stellar halo, reaching to distances of ~ 45 kpc and fully enclosing the stellar stream and the disrupting dwarf galaxy. The halo is asymmetric with a shell-like cut-off at its more extended right side. At least two further objects could be connected to the NGC 0426 system. The galaxy located at $(x = 19$ kpc, $y = -19$ kpc), slightly offset from the presumed centre of the dwarf, seems to be too blue to act as progenitor of parts of the material in the stellar halo. Also the low surface brightness galaxy at $(x = 10$ kpc, $y = -29$ kpc) shows a bluer colour than the stellar halo $((g - i)\sim 0.8)$, although the difference in colour is not too large. At this stage, we cannot
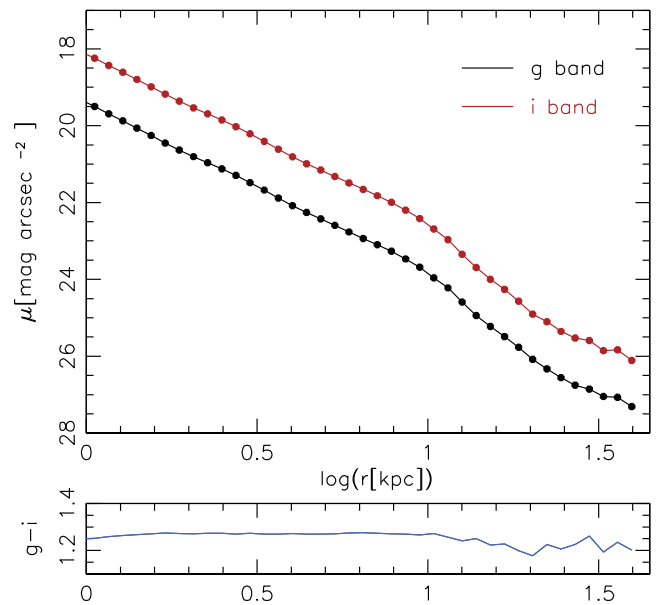

Figure 13. Surface brightness profiles of NGC 0426 in the *g* (black line) and *i* (red line) bands.

confirm nor rule out a connection of those objects with NGC 0426 and its stream system. Spectroscopic follow-up observations providing information on distances and stellar populations will help to disentangle the components and derive the recent accretion history of NGC 0426.

6.3 Low surface brightness galaxies

Recently, a population of extremely diffuse galaxies with central surface brightness $24 \leq \mu(g, 0) \leq 26$ mag arcsec^{-2} has been

identified in the Coma cluster (Koda et al. 2015; van Dokkum et al. 2015). One third of these roughly 1000 UDGs are Milky Way sized with large effective radii of $R_E > 1.5$ kpc, however small stellar masses of only few 10^7–10^8 M$_\odot$. The UDGs have exponential light profiles, effective radii $R_E \sim 0.8$–5 kpc and effective surface brightness $25 \leq \langle \mu_e(R) \rangle \leq 28$ mag arcsec^{-2}. Roughly, 8 per cent have compact nuclei at their centres. As they show a distribution concentrated around the cluster centre, it is very likely that the great majority are indeed cluster members. This is also supported by the fact that the objects are unresolved into stars in agreement with them being at Coma's distance. The UDGs lie along the red sequence in the CMD, consistent with a passively evolving population, which may have lost their gas supply at early times, possibly resulting in very high dark matter fractions (Yozin & Bekki 2015).

The number density of UDGs in different environments is still unknown, possibly most of these galaxies are confined to galaxy clusters where several processes could help to remove the gas and quench star formation. Indeed, first identifications of similar objects were obtained in the Virgo cluster (Sandage & Binggeli 1984). The galaxies which were classified as 'Huge Im or dE' are of huge size (up to 10 kpc in diameter) and very low central surface brightness of about $\mu(B, 0) = 25$ mag arcsec^{-2}. Also the 20 Virgo UDGs show a concentration towards the centre suggesting a cluster membership. Only a small number of large, low surface brightness galaxies are known in the field (Dalcanton et al. 1997; Burkholder, Impey & Sprayberry 2001; Impey, Burkholder & Sprayberry 2001). Another newly detected UDG recently reported in Martínez-Delgado et al. (2015) could reside in the field as well, although this object most probably is associated with a filament of the Pisces-Perseus supercluster and not located in isolation. The object lies at a redshift distance of 78 Mpc, implying an extremely large size ($R_E \sim 4.7$ kpc) for its stellar mass of only a few 10^8 M$_\odot$. Its properties are consistent with those found for UDGs; it shows a red colour ($V - I = 1.0$), shallow Sérsic index ($n_V = 0.68$) and no emission in Hα, typical of dwarf spheroidal galaxies and suggesting that it is mainly composed of old stars.

Low surface brightness UDGs are well within the detectability limit of the co-added Stripe 82 data, also proven by the detection of the presumed progenitor galaxy of the stream around NGC 0936. This will allow one to probe their frequency in field environments for a significant area, and will give new insights into their formation and evolution. The large Stripe 82 area will further shed some light on the abundance of predicted 'dark galaxies' with surface brightness even below the one of UDGs ($\mu_V > 27$ mag arcsec^{-2}). These objects have been predicted within the ΛCDM framework (e.g. Ricotti & Gnedin 2005) but have never been observationally sought, thus possibly remaining hidden from our current surveys of the sky. Galaxies with such extreme low surface brightness will be ideal tracers to explore the properties of almost pure dark matter galaxies.

6.4 Intracluster light

Little is known about the properties of the ICL in galaxy clusters, the diffuse light component extending several hundred kpc from the cluster centre with typical surface brightness $\mu_V \sim 26.5$ mag arcsec^{-2} (e.g. Mihos et al. 2005; Zibetti et al. 2005; Rudick, Mihos & McBride 2006). The ICL is thought to be made up primarily by stars which were tidally stripped from their parent galaxy during interactions and mergers with other cluster galaxies. The formation time-scales of the ICL are pretty much unconstrained; measured metallicities show a wide spread from metal poor to super-solar (e.g.
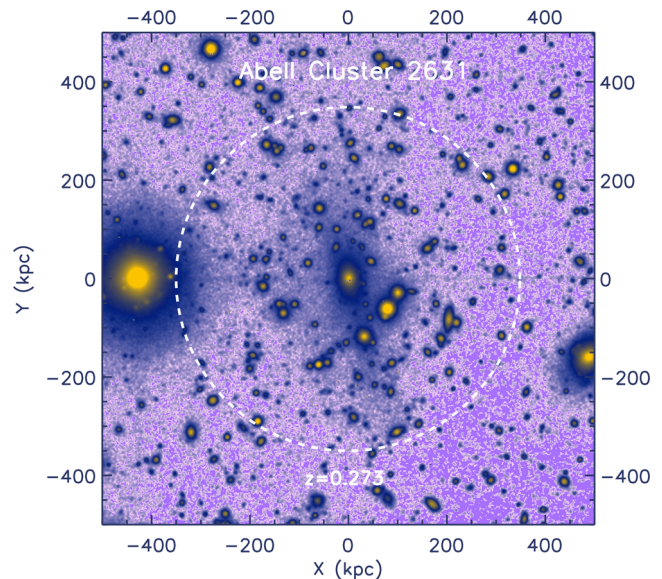

Figure 14. Abell cluster 2631 at $z = 0.273$ as seen in our Stripe 82 r-band co-add. The dashed line encircles a radius of 350 kpc. The image shows the extended ICL of the cluster observed down to the limit of the survey $\mu_r \sim 28.5$ mag arcsec^{-2}.

Durrell et al. 2002; Krick, Bernstein & Pimbblet 2006; Montes & Trujillo 2014). The Stripe 82 co-adds offer the possibility to address these questions and characterize with an unparalleled quality the ICL properties: the quantity of stars in this diffuse component, typical shapes and extensions, and its relation to the entire mass of the galaxy cluster. ΛCDM simulations predict around five massive clusters ($M_{Clu} > 10^{14}$ M$_\odot$) per square degree up to $z\sim0.3$ (Hallman et al. 2007). That means that within Stripe 82 it will be possible to precisely derive the characteristics of the ICL in a sample of around 1300 massive nearby galaxy clusters. Fig. 14 exemplifies the power of our Stripe 82 data for this kind of studies. This figure shows the ICL in the Abell cluster 2631 at $z = 0.273$. The extension of the ICL is clearly visible up to a radius of $\sim$350 kpc from the cluster centre.

6.5 Diffuse Galactic light

First noticed in the late 1930s (e.g. Elvey & Roach 1937; Henyey & Greenstein 1941), the diffuse Galactic light or optical cirrus is starlight scattered off by dust grains in the diffuse interstellar medium (ISM). Reprocessed light is emitted at infrared wavelengths. The comparison between the dust cirrus both in the optical and the infrared would give a powerful tool for probing the dust properties as well as the interstellar radiation field in the ISM (e.g. Beichman 1987; Guhathakurta & Tyson 1989). The Stripe 82 area covers a large contiguous field of the sky ranging from Galactic latitudes $-65° \lesssim b \lesssim -25°$. This allows one to explore in large detail the optical variation of the dust properties from regions closer to the Galactic plane to high Galactic latitudes. Fig. 15 shows a 32 arcmin $\times$ 32 arcmin Stripe 82 field located at intermediate Galactic latitude ($l = 60°.83$, $b = -43°.18$). This r-band image shows obvious dust filaments. The depth and resolution of the Stripe 82 are comparable with current optical studies focused on this astrophysical phenomena (e.g. Ienaka et al. 2013) but the area covered by the survey surpasses by a factor of $\sim$100 the explored area in previous works. Undoubtedly, the analysis of the Stripe 82 data will become a major step forward in the understanding of the ISM. Combining the
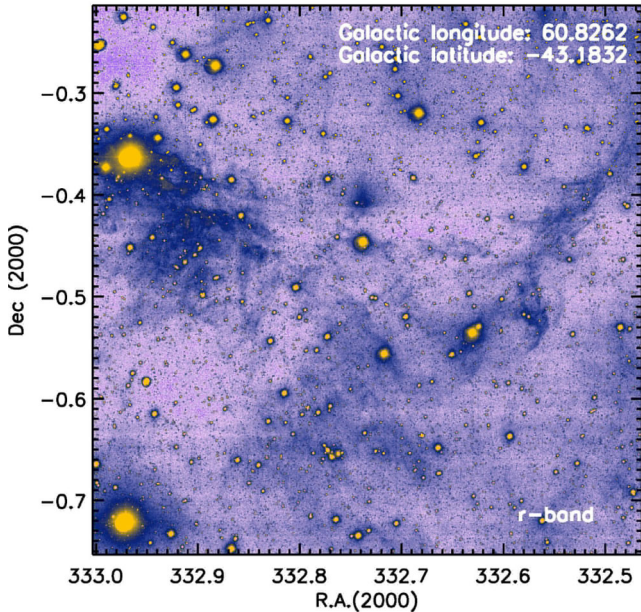
Figure 15. A Stripe 82 field of 32 arcmin × 32 arcmin size showing dust filamentary structure of our Galaxy in the *r* band. The depth and resolution of our imaging allow us to explore faint optical cirrus with exquisite detail.

optical emission with measurements in the UV (*GALEX*; Niemack et al. 2009) and infrared (*Herschel*; Viero et al. 2014) will establish the spectral energy distribution of the cirrus for a large wavelength range. Its shape and its dependences from both the emission strength and the intensity of the radiation field will provide new insights into the emission and heating mechanisms of the Galactic dust clouds. A closer insight into the properties and characteristics of the Galactic dust emission is urgently needed as its range in surface brightness intersects in large parts with the brightness of the aforementioned science cases, from stellar haloes and streams to the ICL. Indeed, Arp's loop, a suspected stream-like ring around M81 suggesting an interaction between M81 and M82, recently turned out to be likely a superposition of a few recent star-forming regions located close to M81, M81's extended disc and Galactic Cirrus emission (Davies et al. 2010; Sollima et al. 2010), the latter being responsible for the diffuse appearance of the feature.

7 CONCLUSIONS

The low surface brightness Universe only recently gathered more attention and started to be investigated in greater detail. Stellar streams around galaxies are now identified and characterized on a regular basis using small- to medium-sized telescopes (e.g. Martínez-Delgado et al. 2008, 2010; Duc et al. 2014; van Dokkum, Abraham & Merritt 2014). Most of these surveys use pointed observations of pre-selected targets and are restricted to a limited field of view.

The Stripe 82 data cover 275 square degrees and reach surface brightness limits $\mu_r \sim 28.5$ mag arcsec^{-2} (3σ, 10 arcsec × 10 arcsec), comparable to the one's acquired in the aforementioned studies. In this way, it can be used as a blind survey allowing statistical tests of the frequency and characteristics of low surface brightness phenomena like UDGs, stellar streams, extended discs or tidal interactions for different types of galaxies.

In our reduction of the Stripe 82 data, we put special emphasis on preserving the characteristics of the low surface brightness structures on all spatial and intensity scales. Our effort is made publicly

available through a webpage at http://www.iac.es/proyecto/stripe82. The data release includes the co-added data in 5+1 bands (u, g, r, i, z, $r_{\mathrm{deep}} = \langle g+r+i \rangle$), corresponding exposure time maps and image representations of the PSF. We also provide separate source catalogues for point and extended objects with stars and galaxies confidently separated until $g \sim 23$ mag. Our completeness simulations showed that for exponential profiles the data are 50 per cent complete at the 3σ level for an effective surface brightness $\langle \mu_e(r) \rangle \sim 25.5$ mag arcsec^{-2}. The 50 per cent completeness limits for point sources are (24.2, 25.2, 24.7, 24.3, 23.0) mag in (u, g, r, i, z), reaching between 0.1 and 0.3 mag deeper than the reduction of Annis et al. (2014) while being at the same depth as Jiang et al. (2014).

Discoveries like the faint stellar streams around NGC 0936 and NGC 0426 in our data give a glimpse of the prospects of deep wide-field surveys like Stripe 82 for the study of the, until now almost hidden, low surface brightness Universe. The full exploration of the Stripe 82 data set, including its extensions to wavebands from the UV to the infrared, will have the possibilities to add significant pieces of new insights to this relatively new research field.

REFERENCES

Abazajian K. N. et al., 2009, ApJS, 182, 543
Annis J. et al., 2014, ApJ, 794, 120
Bakos J., Trujillo I., 2012, preprint (arXiv:1204.3082)
Beichman C. A., 1987, ARA&A, 25, 521
Bertin E., 2011, in Evans I. N., Accomazzi A., Mink D. J., Rots A. H., eds, ASP Conf. Ser. Vol. 442, Astronomical Data Analysis Software and Systems XX. Astron. Soc. Pac., San Francisco, p. 435
Bertin E., Arnouts S., 1996, A&AS, 117, 393
Bertin E., Mellier Y., Radovich M., Missonnier G., Didelon P., Morin B., 2002, in Bohlender D. A., Durand D., Handley T. H., eds, ASP Conf. Ser. Vol. 281, Astronomical Data Analysis Software and Systems XI. Astron. Soc. Pac., San Francisco, p. 228
Bullock J. S., Johnston K. V., 2005, ApJ, 635, 931

Burkholder V., Impey C., Sprayberry D., 2001, AJ, 122, 2318

Contini E., De Lucia G., Villalobos Á., Borgani S., 2014, MNRAS, 437, 3787

Cooper A. P. et al., 2010, MNRAS, 406, 744

Cuillandre J.-C. J. et al., 2012, Proc. SPIE, 8448, 84480M

Dalcanton J. J., Spergel D. N., Gunn J. E., Schmidt M., Schneider D. P., 1997, AJ, 114, 635

Davies J. I. et al., 2010, MNRAS, 409, 102

de Vries C. P., Le Poole R. S., 1985, A&A, 145, L7

Duc P.-A., Paudel S., McDermid R. M., Cuillandre J.-C., Serra P., Bournaud F., Cappellari M., Emsellem E., 2014, MNRAS, 440, 1458

Durrell P. R., Ciardullo R., Feldmeier J. J., Jacoby G. H., Sigurdsson S., 2002, ApJ, 570, 119

Eggen O. J., Lynden-Bell D., Sandage A. R., 1962, ApJ, 136, 748

Elvey C. T., Roach F. E., 1937, ApJ, 85, 213

Erwin P., 2015, ApJ, 799, 226

Fall S. M., Efstathiou G., 1980, MNRAS, 193, 189

Ferguson A. M. N., Irwin M. J., Ibata R. A., Lewis G. F., Tanvir N. R., 2002, AJ, 124, 1452

Ferrarese L. et al., 2012, ApJS, 200, 4

Font A. S. et al., 2011, MNRAS, 417, 1260

Frieman J. A. et al., 2008, AJ, 135, 338

Giallongo E. et al., 2014, ApJ, 781, 24

Guhathakurta P., Tyson J. A., 1989, ApJ, 346, 773

Hallman E. J., O'Shea B. W., Burns J. O., Norman M. L., Harkness R., Wagner R., 2007, ApJ, 671, 27

Henyey L. G., Greenstein J. L., 1941, ApJ, 93, 70

Ienaka N., Kawara K., Matsuoka Y., Sameshima H., Oyabu S., Tsujimoto T., Peterson B. A., 2013, ApJ, 767, 80

Impey C., Burkholder V., Sprayberry D., 2001, AJ, 122, 2341

Ivezić Ž. et al., 2007, AJ, 134, 973

Jiang L. et al., 2008, AJ, 135, 1057

Jiang L. et al., 2014, ApJS, 213, 12

Kennicutt R. C., Jr, 1989, ApJ, 344, 685

Koda J., Yagi M., Yamanoi H., Komiyama Y., 2015, ApJ, 807, L2

Krick J. E., Bernstein R. A., Pimbblet K. A., 2006, AJ, 131, 168

Low F. J. et al., 1984, ApJ, 278, L19

McConnachie A. W., Chapman S. C., Ibata R. A., Ferguson A. M. N., Irwin M. J., Lewis G. F., Tanvir N. R., Martin N., 2006, ApJ, 647, L25

McConnachie A. W. et al., 2009, Nature, 461, 66

Martín-Navarro I., Trujillo I., Knapen J. H., Bakos J., Fliri J., 2014, MNRAS, 441, 2809

Martínez-Delgado D., Peñarrubia J., Gabany R. J., Trujillo I., Majewski S. R., Pohlen M., 2008, ApJ, 689, 184

Martínez-Delgado D. et al., 2010, AJ, 140, 962

Martínez-Delgado D. et al., 2015, submitted

Merritt A., van Dokkum P., Abraham R., 2014, ApJ, 787, L37

Mihos J. C., Harding P., Feldmeier J., Morrison H., 2005, ApJ, 631, L41

Monet D. G. et al., 2003, AJ, 125, 984

Montes M., Trujillo I., 2014, ApJ, 794, 137

Mouhcine M., Ferguson H. C., Rich R. M., Brown T. M., Smith T. E., 2005, ApJ, 633, 821

Mouhcine M., Rejkuba M., Ibata R., 2007, MNRAS, 381, 873

Niemack M. D., Jimenez R., Verde L., Menanteau F., Panter B., Spergel D., 2009, ApJ, 690, 89

Paley E. S., Low F. J., McGraw J. T., Cutri R. M., Rix H.-W., 1991, ApJ, 376, 335

Peng C. Y., Ho L. C., Impey C. D., Rix H.-W., 2002, AJ, 124, 266

Peters S. P. C., van der Kruit P. C., Knapen J. H., Trujillo I., Fliri I., Cisternas M., Kelvin L., 2015, submitted

Pier J. R., Munn J. A., Hindsley R. B., Hennessy G. S., Kent S. M., Lupton R. H., Ivezić Ž., 2003, AJ, 125, 1559

Pohlen M., Trujillo I., 2006, A&A, 454, 759

Radburn-Smith D. J. et al., 2011, ApJS, 195, 18

Ricotti M., Gnedin N. Y., 2005, ApJ, 629, 259

Rudick C. S., Mihos J. C., McBride C., 2006, ApJ, 648, 936

Rudick C. S., Mihos J. C., Harding P., Feldmeier J. J., Janowiecki S., Morrison H. L., 2010, ApJ, 720, 569

Sandage A., Binggeli B., 1984, AJ, 89, 919

Sandin C., 2014, A&A, 567, A97

Schaye J., 2004, ApJ, 609, 667

Schlegel D. J., Finkbeiner D. P., Davis M., 1998, ApJ, 500, 525

Searle L., Zinn R., 1978, ApJ, 225, 357

Sollima A., Gil de Paz A., Martinez-Delgado D., Gabany R. J., Gallego-Laborda J. J., Hallas T., 2010, A&A, 516, A83

Stetson P. B., 1987, PASP, 99, 191

Tissera P. B., Scannapieco C., Beers T. C., Carollo D., 2013, MNRAS, 432, 3391

Trujillo I., Fliri J., 2015, preprint (arXiv:1510.04696)

van der Kruit P. C., 1979, A&AS, 38, 15

van der Kruit P. C., 1987, A&A, 173, 59

van Dokkum P. G., Abraham R., Merritt A., 2014, ApJ, 782, L24

van Dokkum P. G., Abraham R., Merritt A., Zhang J., Geha M., Conroy C., 2015, ApJ, 798, L45

Viero M. P. et al., 2014, ApJS, 210, 22

York D. G. et al., 2000, AJ, 120, 1579

Yozin C., Bekki K., 2015, MNRAS, 452, 937

Zibetti S., White S. D. M., Brinkmann J., 2004, MNRAS, 347, 556

Zibetti S., White S. D. M., Schneider D. P., Brinkmann J., 2005, MNRAS, 358, 949

This paper has been typeset from a TEX/LATEX file prepared by the author.